



Dynamic Observing and Tiling Strategies for the DESI Legacy Surveys

Kaylan J. Burleigh^{1,2}, Martin Landriau², Arjun Dey³, Dustin Lang^{4,5}, David J. Schlegel², Peter E. Nugent^{1,2}, Robert Blum³, Joseph R. Findlay⁶, Douglas P. Finkbeiner⁷, David Herrera³, Klaus Honscheid⁸, Stéphanie Juneau³, Ian McGreer⁹, Aaron M. Meisner³, John Moustakas¹⁰, Adam D. Myers⁶, Anna Patej¹¹, Edward F. Schlafly¹², Francisco Valdes³, Alistair R. Walker¹³, Benjamin A. Weaver³, and Christophe Yèche¹⁴
and the DECaLS, MzLS, and BASS Teams

¹ Department of Astronomy, University of California at Berkeley 501 Campbell Hall #3411, Berkeley, CA 94720, USA

² Lawrence Berkeley National Laboratory One Cyclotron Road, Berkeley, CA 94720, USA; mlandriau@lbl.gov

³ NSF's Optical-Infrared Astronomy Research Laboratory P.O. Box 26732, Tucson, AZ 85719, USA

⁴ Perimeter Institute for Theoretical Physics, 31 Caroline Street N, Waterloo, Ontario, N2L 2Y5, Canada

⁵ Department of Physics and Astronomy, University of Waterloo, Waterloo, ON N2L 3G1, Canada

⁶ Department of Physics & Astronomy University of Wyoming, 1000 E. University, Dept. 3905, Laramie, WY 82071, USA

⁷ Harvard-Smithsonian Center for Astrophysics Harvard University, 60 Garden Street, Cambridge, MA 02138, USA

⁸ Department of Physics, Ohio State University 191 West Woodruff Avenue, Columbus, OH 43210, USA

⁹ Steward Observatory, University of Arizona 933 N. Cherry Avenue, Tucson, AZ 85721, USA

¹⁰ Department of Physics & Astronomy, Siena College 515 Loudon Road, Loudonville, NY 12211, USA

¹¹ Stanford Law School, 559 Nathan Abbott Way, Stanford, CA 94305, USA

¹² Lawrence Livermore National Laboratory 7000 East Avenue, Livermore, CA 94550, USA

¹³ Cerro Tololo Inter-American Observatory, NSF's Optical-Infrared Astronomy Research Laboratory Casilla 603, La Serena, Chile

¹⁴ CEA, Centre de Saclay, IRFU/DPhP, F-91191 Gif-sur-Yvette, France

Received 2020 February 13; revised 2020 May 12; accepted 2020 May 15; published 2020 July 9

Abstract

The Dark Energy Spectroscopic Instrument Legacy Surveys, a combination of three ground-based imaging surveys, have mapped 16,000 deg² in three optical bands (g , r , and z) to a depth 1–2 mag deeper than the Sloan Digital Sky Survey. Our work addresses one of the major challenges of wide-field imaging surveys conducted at ground-based observatories: the varying depth that results from varying observing conditions at Earth-bound sites. To mitigate these effects, the Legacy Surveys (the Dark Energy Camera Legacy Survey, or DECaLS; the Mayall z -band Legacy Survey, or MzLS; and the Beijing-Arizona Sky Survey, or BASS) employed a unique strategy to dynamically adjust the exposure times as rapidly as possible in response to the changing observing conditions. We present the tiling and observing strategies used by the first two of these surveys. We demonstrate that the tiling and dynamic observing strategies jointly result in a more uniform-depth survey that has higher efficiency for a given total observing time compared with the traditional approach of using fixed exposure times.

Unified Astronomy Thesaurus concepts: Sky surveys (1464); Astronomical methods (1043)

1. Introduction

The Legacy Surveys¹⁵ (see Zou et al. 2017; Dey et al. 2019) are a combination of three imaging surveys that have mapped two contiguous areas totaling 16,000 deg² in three optical bands (g , r , and z) to depths 1–2 mag deeper than the Sloan Digital Sky Survey imaging (SDSS; e.g., Abazajian et al. 2009). The three surveys that make up the Legacy Surveys are the DECam Legacy Survey (DECaLS), the Mayall z -band Legacy Survey (MzLS), and the Beijing-Arizona Sky Survey (BASS). DECaLS uses the Blanco 4 m telescope and Dark Energy Camera (DECam; Flaugher et al. 2015) located at Cerro Tololo, Chile; MzLS uses the Mosaic3 camera (Dey et al. 2016) at the Mayall Telescope located at Kitt Peak in Arizona; and BASS uses the Bok 2.3 m telescope/90Prime camera on Kitt Peak (Williams et al. 2004). MzLS was completed in early 2018 and the other two surveys were completed in early 2019. The Legacy Surveys also provide mid-infrared photometric measurements for all optical sources derived using forced photometry on coadded multi-epoch data from the Wide-field Infrared Survey Explorer (WISE; Wright et al. 2010).

The primary purpose of the Legacy Surveys is to provide targets for the Dark Energy Spectroscopic Instrument (DESI; DESI Collaboration et al. 2016a, 2016b). DESI is a robotically actuated 5000-fiber spectrograph that will survey 14,000 deg² of sky in order to make a Stage IV measurement of dark energy. Spectra and redshifts of more than 30 million galaxies and quasars will be obtained over this five-year survey. DESI, installed at the prime focus of the Mayall 4 m telescope on Kitt Peak, Arizona, is currently being commissioned and will begin survey operations in 2021.

In addition to providing targets for DESI, the Legacy Surveys have already dramatically improved the utility of existing spectroscopic and imaging data sets, by spanning the SDSS footprint and being 1–2 mag deeper, with better image quality, than either the SDSS or the Panoramic Survey Telescope and Rapid Response System 1 (Pan-STARRS 1, or PS1) 3π survey (Chambers et al. 2016). Existing spectroscopic data sets in the DESI footprint include SDSS, the Two-degree-Field Galaxy Redshift Survey, and the WiggleZ Dark Energy Survey. Increasing g -, r -, and z -band depths by 1.5–2 mag, increases the number of $z > 0.5$ galaxies with imaging measurements by about a factor of 30. No other ongoing or currently planned ground-based survey will provide this depth or uniformity of depth over as large an extragalactic (i.e.,

¹⁵ <http://legacysurvey.org>

Table 1
Camera Properties

Camera	CCDs	Amplifiers (per CCD)	Pixels (per CCD)	Pixel Scale	FOV (deg ²)	Fill Factor
DECam	62	2	4094 × 2046	0.262	3.18	0.87
Mosaic3	4	4	4079 × 4054	0.260	0.36	0.95
90Prime	4	4	4096 × 4032	0.455	1.16 × 1.16	0.94

Note. Pixel scale: arcsec pixel⁻¹. FOV: camera field of view including CCD gaps and dead CCDs. Fill factor: fraction of the field of view that is covered by CCDs.

$|b| \geq 20^\circ$) footprint as the Legacy Surveys, especially in the northern hemisphere. For example, the Dark Energy Survey has observed 5000 deg² of the southern sky, overlapping only about 1000 deg² of the SDSS footprint (The Dark Energy Survey Collaboration 2005).

All previous ground-based wide-field imaging surveys have used fixed exposure times per band, which result in survey depths that vary across the survey footprint due to both terrestrial and extraterrestrial constraints. Terrestrial constraints include the observing conditions (i.e., cloud cover, transparency, delivered image quality, sky brightness) and telescope limitations (e.g., zenith distance of observation, telescope pointing accuracy, telescope tracking accuracy, focus, etc.). Extraterrestrial constraints include the extinction due to Galactic and solar system dust, zodiacal dust, sky brightness, Galactic cirrus and other sources of diffuse emission, and source crowding. Cosmological surveys require a uniformity of depth over a large area, and hence imaging surveys with varying depth are generally truncated near their shallowest depth or are subjected to uncertain completeness corrections.

In this paper, we describe the innovative approach employed in our observing strategy for DECaLS and MzLS (the observing strategy for BASS is presented in Zou et al. 2017). Instead of adopting a fixed exposure time, we analyzed images contemporaneously in order to dynamically adjust the exposure time to ensure a near-constant depth for each image. This procedure allowed us to optimally use the available telescope time with the minimum of reobservation. This optimization was particularly important given that the imaging surveys had to be completed to a minimum depth in less than four years due to the DESI construction and installation schedule.

The paper is organized as follows. In Section 2, we present the choices of tiling for DECaLS and MzLS. In Section 3, we describe the goals of our observing strategy. In Section 4, we discuss how we implemented dynamic observing.

2. Tiling Strategy

2.1. General Concepts

Wide-field imaging surveys typically aim to cover one or more contiguous areas of sky much larger than the footprint of the imaging camera. The Legacy Surveys represent a particularly extreme case where we have imaged a 16,000 deg² region using cameras that have fields of view of between 0.36 and 3.18 deg² (see Table 1). In addition, all of the camera focal planes are CCD mosaics that have gaps between individual CCDs. Hence, an efficient tiling pattern has to both cover the entire area with as few tiles as possible, and also cover all of the CCD gaps to some minimum depth driven by the science requirements.

Once the basic tiling strategy was identified, we defined a total of three independent tilings, with each tiling offset from

Table 2
Tiling Solutions for DECaLS and MzLS

N	DECaLS	MzLS
0	1.0000	1.0000
1	0.9998	1.0000
2	0.9801	0.9950
3	0.7443	0.8500

Note. The DECaLS and MzLS columns are the fraction of the sky footprint having a given number of repeat exposures (N).

the other two by some prescribed amount. Three tilings ensure that the footprint is almost entirely covered, while also minimizing the amount of area that does not have at least two images at any given position. Two-pass coverage is useful both to discriminate and mask any particle events or other detector-based anomalies, and to boost the signal-to-noise ratio (S/N) compared to a single pass. We used a Monte Carlo process of different offsets for the tiling sets for each camera in order to select the offsets that maximized three-pass coverage while minimizing one-pass coverage.

The detailed implementations for each camera are described in the following two subsections.

2.2. Implementation for DECaLS

DECam has a roughly circular field of view of $a_{\text{FOV}} = 3.18 \text{ deg}^2$ (Flaugher et al. 2015). To cover the entire sky, the ideal tiling would require $N = 4\pi(180/\pi)^2/a_{\text{FOV}} = 12,973$ tiles (not accounting for CCD gaps or nonworking CCDs, see Table 1).

For defining the tiling for DECaLS, we adopted the approach of Hardin et al. (2012), who considered the general problem of covering a sphere uniformly with a fixed number of points. We selected the precomputed icosahedral arrangements of Hardin et al. (2012) with tiling N_{tile} that was close in number to but greater than N (i.e., the minimum number while still providing sufficient overlap with the neighboring tile). We investigated the icosahedral tilings with $N_{\text{tile}} = [15,252, 15,392, 15,872, 16,002, 16,472, 16,752]$ and settled on $N = 15,872$ as providing the best solution with 99.98% and 98.01% of the sky having at least two and three exposures respectively, using a three-pass strategy.

Two of the three passes are copies of the first pass, offset by $[\Delta R.A., \Delta \text{decl.}]$ of $[0.2917, 0.0833] \text{ deg}$ and $[0.5861, 0.1333] \text{ deg}$ respectively. This solution results in fractional coverage within the DESI footprint as shown in Table 2. Ideally, we would obtain three-image coverage of 100%, but this is not possible with a three-pass strategy given the gaps between the DECam CCDs. The resulting tiling for DECaLS is shown in Figure 1 along with the as-observed coverage

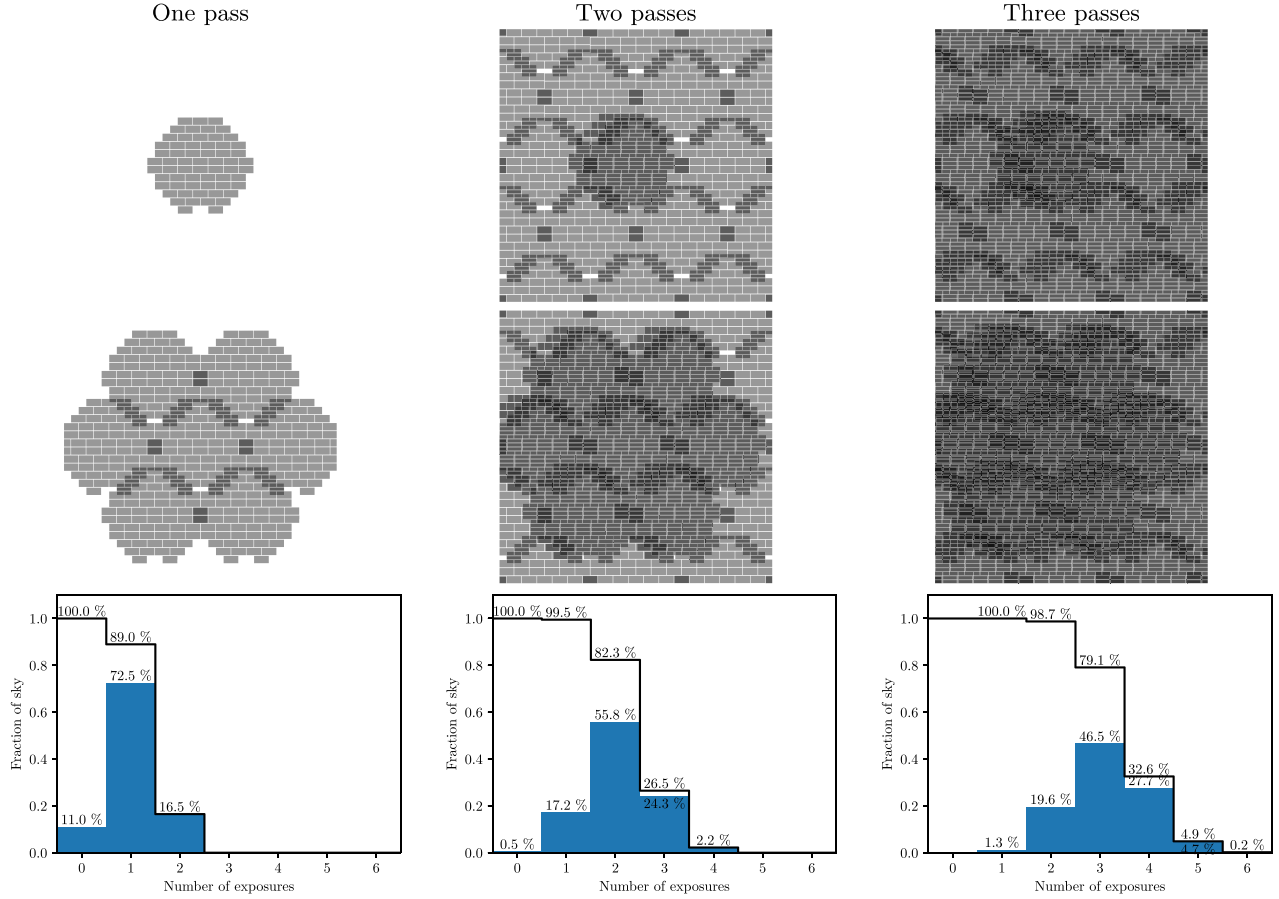


Figure 1. Tiling strategy in the DECaLS survey. DECam has 62 science CCDs, but during the course of the survey, one or two CCDs have been inoperative. In the example exposure shown, CCD N30 is inoperative, leaving a hole in the edge of the hexagonal footprint. The first column shows a region of sky (about 5.5° wide) covered with our Pass 1 tiling, with a single exposure in the top row and neighboring tiles in the second row. The bottom row shows the approximate coverage statistics, where the x-axis represents the number of repeat exposures. The black lines should be compared to the numbers in Table 2 and show the fraction of sky that have at least $N + 1$ exposures; the difference between the Pass 3 numbers and those in the table result mainly from small pointing errors. The blue histograms show the fraction of sky that only have $N + 1$ exposures. The second and third columns show the coverage after our Pass 2 and Pass 3 tilings have been added, respectively.

statistics (which include pointing errors during the observations).

2.3. Implementation for MzLS

The Mosaic3 Camera has an approximately square on-sky footprint with a field of view of $35.89' \times 36.06'$ (Table 1; see also Dey et al. 2016). Given the smaller size and roughly square footprint, we settled on a tiling pattern that was aligned along rows of constant decl., with adjacent frames overlapping by $1.7'$ on all four sides. The resulting map has 122,765 tile centers in a single pass; the two other passes are offset by $11.7'$ and $23.5'$ in decl., respectively (or one-third and two-third of the field of view).

This choice of tiling ensures that 99.5% of the footprint is covered by at least three exposures (see Table 2). The tiling for MzLS is shown in Figure 2 along with the as-observed coverage statistics.

3. Observing Strategy

3.1. Optimizing for Photometric Calibration and Image Quality

Three passes, each constituting a complete tiling of the footprint as described in the previous section, were chosen to maximize the scientific uniformity and utility of the survey. In order to ensure that a given survey could be photometrically

calibrated, we reserved the first tiling of the footprint (Pass 1) for times with photometric conditions when the seeing was good (i.e., $<1.3''$). We reserved the second tiling (Pass 2) for times with *either* photometric conditions *or* good seeing. We reserved the third tiling (Pass 3) for times when neither of these conditions were met, but were still deemed acceptable, i.e., seeing $<2''$, transparency >0.9 , and sky brightness no more than 0.25 mag brighter than the nominal value for that band. This strategy was designed to ensure that every point within the survey footprint had at least one image that could be photometrically calibrated and at least one image that had good seeing. We observed three passes across the entire survey footprint to ensure the high completeness in two passes across every point in the footprint. During times when the weather was poor (i.e., worse than Pass 3 conditions), we still took data when possible, but these data did not contribute to the final catalogs.

3.2. Optimizing the Nightly Plan

As much as possible, we scheduled z-band observations during bright time (i.e., when the Moon was above the horizon, or the Sun's altitude was between -10° and -15°) and reserved dark time for *g* and *r*. With these constraints on the Sun and Moon imposed, dark-time and bright-time observations were then planned independently.

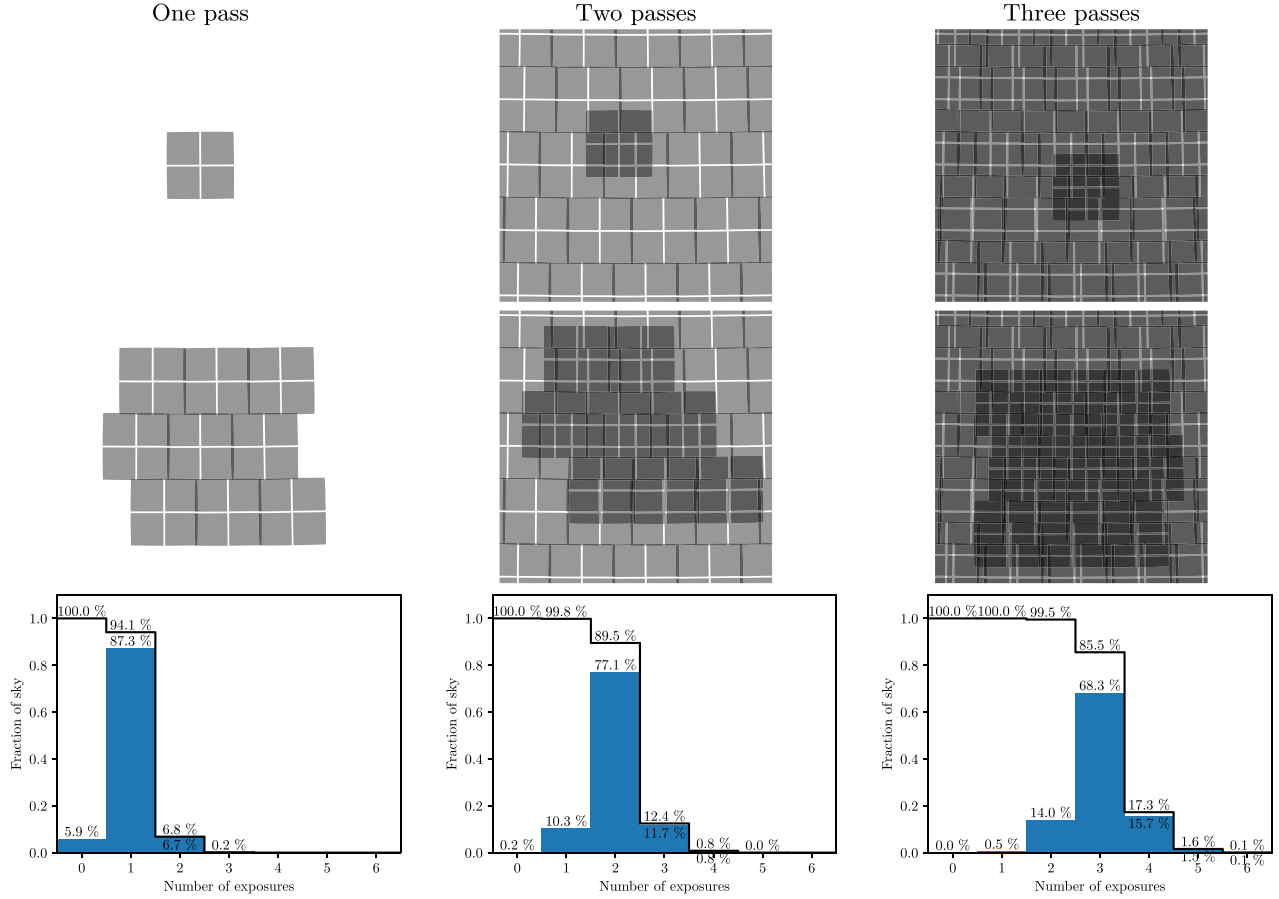


Figure 2. Tiling strategy in the MzLS survey. The Mosaic3 camera has four CCDs, each with a field of view about $0.3^\circ \times 0.3^\circ$, with small gaps between the CCDs. The first column shows a region of sky (about 2.5° wide) covered with our Pass 1 tiling, with a single exposure in the top row and neighboring tiles in the second row. The bottom row shows the approximate coverage statistics, where the x -axis represents the number of repeat exposures. The black lines should be compared to the numbers in Table 2 and show the fraction of sky that have at least $N + 1$ exposures; the difference between the Pass 3 numbers and those in the table result mainly from small pointing errors. The blue histograms show the fraction of sky that only have $N + 1$ exposures. The second and third columns show the coverage after our Pass 2 and Pass 3 tilings have been added, respectively.

In addition, at all times, we restricted observations to airmass ≤ 2.4 and to pointings that were separated from the Moon by at least 40° – 50° , with the exact separation determined by the Moon’s phase. We also avoided observing tiles within 1.2° of bright planets. We enforced minimum and maximum exposure times (see Table 3) to ensure that we did not exceed depth when observing conditions were excellent, and to prevent saturation when the sky was too bright and curtail long exposures in otherwise poor conditions.

The basic logic we adopted is as follows.

1. Tag tiles with bad exposures as unobserved.
2. Rank order by R.A. and split unobserved tiles by filter.
3. Remove tiles that are too close to the median position of the Moon and planets (Mars–Neptune) over the night.
4. Rank order the list of future observing nights, starting with the desired night, by local mean sidereal time (LMST) and then split each night into one-minute-spaced intervals in LMST.
5. Split the LMST list into dark and bright time.
6. For bright and dark time respectively, match the rank-ordered R.A. and LMST lists by minimizing the time difference between them.
7. Retain LMSTs that are within 5° of each R.A.

	Fiducial	Min	Max
MzLS & DECaLS- z	100	80	250
DECaLS- g	70	56	200
DECaLS- r	50	40	175

8. *The annealing process:* randomly swap the LMST of two tiles. Accept the new positions if the total airmass is reduced. Repeat 400 times.
9. *For DECaLS only:* prioritize the tiles for building that night’s plan. Observations are chosen preferentially at decl. near decl. = 0, with a penalty of $1/100.0$ per deg away from the equator. Also prioritize selecting tiles near the last observation, with a penalty of $1/10.0$ per deg for distances more than 2° away. Priorities are increased (doubled) for observations of tiles that have been previously observed in at least one other filter. Increase priority for observations of the same tile. This should preferentially schedule pairs of $g + r$ exposures in dark time. Priorities set to zero for tiles within 1.20° of Mars–Neptune.
10. Build the plan for the night. Pass 1 is preferentially selecting Pass 1 tiles, then Pass 2, then Pass 3, then a

repeat observation of an already-observed tile. Pass 2 is preferentially selecting Pass 2 tiles, then Pass 3, etc.

11. Observations begin and end at 12° twilight for DECaLS and 10° for MzLS.
12. *The untangling process*: reduce slews by splitting tiles into blocks (consecutive tiles having slews $>5^\circ$) and then trying all permutations of the blocks. After this the tiles are split again, using blocks of eight consecutive tiles, and the best permutation is chosen.
13. Create a list of reserve tiles for bright and dark time from the list of observed and unobserved tiles that are closest to transit and sufficiently far from the Moon and planets.
14. Observe tiles at their assigned LMST.

4. Dynamic Observing

4.1. General Concepts

Observing conditions at ground-based observatories change due to temporal and spatial changes in atmospheric transparency and stability, thermal imbalances between the telescope, dome and ambient environment, and the spatial location of celestial objects at the time during which they are observed.

In an ideal world, observing conditions can be monitored during each on-sky integration as it is in progress, and the total duration of the ongoing exposure can be modified in real time to ensure that the image being taken reaches the appropriate depth. This could be accomplished using, say, nondestructive reads to monitor the actual image data as it is being collected, or alternatively using some proxy to estimate the current conditions in the region (e.g., a guide or photometric camera co-located with the telescope and pointed at the same spot in the sky).

The hardware realities of the Mosaic3 and DECam instruments prevented us from implementing any real-time exposure control. However, we were able to implement the next best option: to analyze each image as soon as it was taken, estimate the image quality, transparency, resulting depth and telescope pointing offset, and then adjust our exposure time as soon as possible, typically with a lag of 1 or 2 images.

At both the Mayall and Blanco telescopes, dynamic exposures were implemented using two (Python) software “bots”; both monitored the observing conditions and telescope pointing offsets, with one (*copilot*) providing a graphical view of the derived estimates and the other (*decbot/mosbot* in the cases of DECam/Mosaic3, respectively) writing the required scripts and interfacing with the instrument to modify the exposure time. These codes are all publicly available.¹⁶ We describe the individual pieces of this process below.

4.2. Copilot: A Graphical Display

For each raw image, *copilot* measures the seeing, sky brightness, atmospheric transparency, and photometric zero-point. The bot extrapolates from the central 1000×1000 pixels of a single CCD or amplifier (CCD N4 for DECam and amplifier IM4 for Mosaic3) to infer statistics for the entire exposure. For the observers, *copilot* displays plots of seeing, sky brightness, transparency, and R.A. and decl. offsets. Figure 3 shows the summary plot from 2017 March 30.

The combination of *copilot* and either *mosbot* or *decbot* performs on-the-fly image reductions, which we describe briefly below.

Detrending. The first step is to apply bias and gain, and then to estimate the sky level by sigma-clipping the central pixels. This provides a measure of the sky brightness m_{sky} , assuming the canonical zero-point for the given camera and filter.

Source detection. We correlate the image with a matched filter consisting of a 2D Gaussian with a FWHM of 5 pixels, and flagging pixels with $S/N \geq 20 \sigma_{\text{sky}}$. Aperture photometry is carried out for these (unresolved or star-like) sources using an aperture with a diameter of $7''$ (constant pixel scale) and a sky annulus with a diameter of $14''$ – $20''$ (constant pixel scale). The source counts (N_{e-}) are then counts in the object aperture minus the mode of sky annulus times the area of the object aperture. The following restrictions were applied to ensure a clean sample of sources:

1. $N_{e-} > 0$;
2. $12 < m_{\text{AB}} < 22$;
3. at least $11''$ (40 pixels) from CCD edges and any other sources;
4. and no bad pixels within 5 pixels of the centroid.

Seeing quality determination. We estimate the seeing by fitting a circular 2D Gaussian to all sources with $20 < S/N < 100$, where noise includes the Poisson noise from both the sky and the source, and only the FWHM is allowed to vary. The seeing we record is the median of the best-fit FWHM values.

On-the-fly photometric calibration. We compute photometric zero-points relative to the PS1 catalogs, and astrometric offsets from the Gaia DR1 catalogs (Gaia Collaboration et al. 2016a, 2016b). Note that we actually use a single PS1–Gaia catalog, created using a $3.5''$ matching radius. There are occasional holes in the Gaia DR1 catalog in regions that contain plenty of bonafide PS1 stars, so our astrometry reverts to only using PS1 in such regions. We enforce the following constraints on the PS1–Gaia catalog:

1. there can only be exactly one match between the catalogs;
2. the PS1 catalog must not flag the source, in the g , r , and z bands as coming from a bad CCD region, containing bad pixels, or having NaN fluxes;
3. and sources must have a star-like color in the range of $0.4 < g - r < 2.7$, where $g - r$ denotes the PS1 median point-spread function (PSF) magnitude color.

The instrumental zero-point is the difference between the PS1 magnitude of a source (m_{PS1}) and our measured aperture magnitude (m_{AB}), and the 2.5σ -clipped median for all sources in a CCD,

$$ZP = \text{Med}(m_{\text{PS1}} - m_{\text{AB}}) + ZP_0, \quad (1)$$

where ZP_0 is a band-dependent fiducial zero-point we obtained during nights with excellent conditions near the start of the DECaLS and MzLS observations. The relative atmospheric transparency, i.e., the fraction of light that penetrates Earth’s atmosphere relative to a good night at the start of the survey, can then be computed from the zero-point

$$T_{\text{rel}} = 10^{-0.4[ZP_0 - ZP - K(X-1)]}, \quad (2)$$

where K is the atmospheric extinction coefficient and X is the airmass.

¹⁶ <https://github.com/legacysurvey/obsbot>

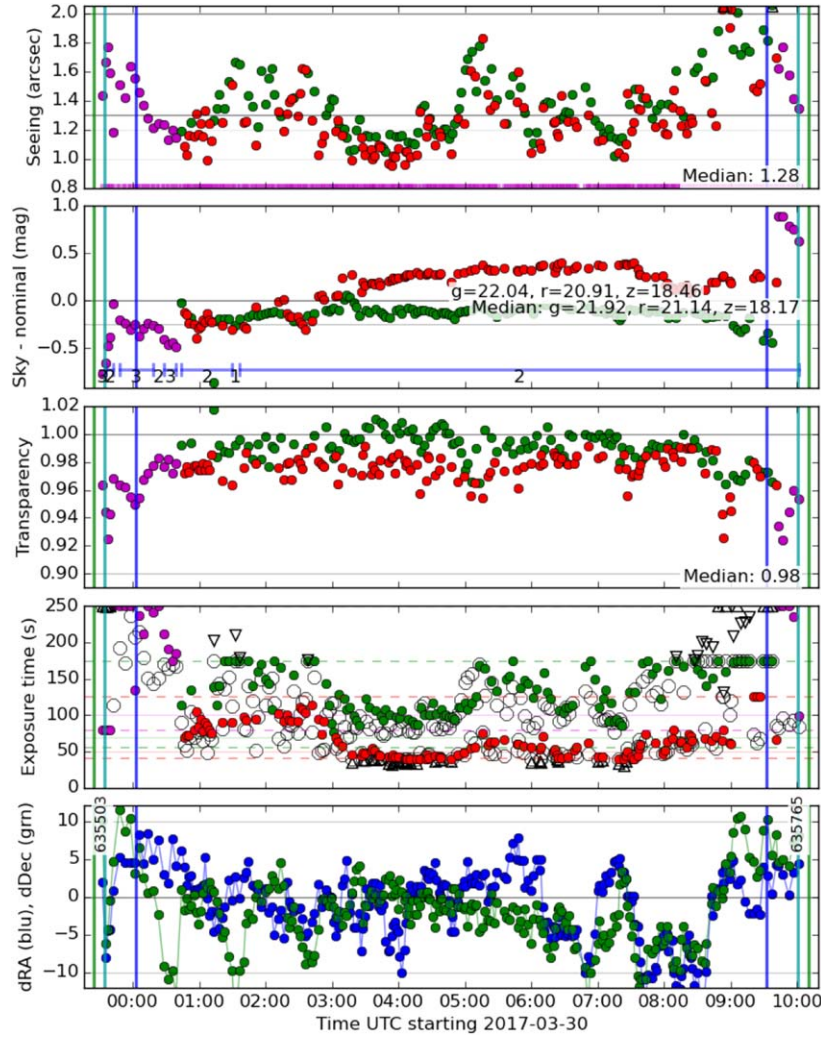


Figure 3. Copilot summary plot for DECaLS night of 2017 March 30.

Depth and exposure factor estimates. The 5σ AB magnitude depth, with Galactic extinction $AE(B - V)$ removed, is

$$m_{\text{depth}} = -2.5 \log_{10} \left(\frac{5\sigma_{\text{sky,eff}}}{t_{\text{exp}}} \right) + ZP - AE(B - V), \quad (3)$$

where $\sigma_{\text{sky,eff}}$ is the square root of sky counts from a region having the size of the source,

$$\sigma_{\text{sky,eff}} = \sqrt{\sigma_{\text{sky}}^2 N_{\text{eff}}}, \quad (4)$$

where N_{eff} is the noise equivalent area, i.e., the effective number of pixels of an astrophysical source on the CCD, given by

$$N_{\text{eff}} = \left(\sum_i v_i \right)^2 / \sum_i v_i^2, \quad (5)$$

where v_i is the pixelized PSF centered on the source. If the source is an extended object, then v_i is the value of the PSF convolved with the object's surface brightness profile. For speed of computation, *copilot* uses an approximation for N_{eff} instead:

$$\hat{N}_{\text{eff}} \approx 4\pi\sigma_{\text{see}}^2 + 8.91r_{\text{half}}^2 + P_{\text{sc}}^2/12, \quad (6)$$

where $r_{\text{half}} = 0.4''$ for extended sources and $r_{\text{half}} = 0''$ for point-sources, and P_{sc} is the plate scale. This approximation is based on the assumption that the seeing is Gaussian, which results in slightly underpredicting the true value of N_{eff} since the seeing profile has larger wings. In fact, this approximation systematically underestimates the true N_{eff} by 20%–40%, but we have found that a linear model ($A\hat{N}_{\text{eff}} + B$) for each camera and point-source/extended source pair agrees well with the true N_{eff} .

Combining Equations (2)–(4), we obtain the exposure time scaling factor relative to its value under nominal conditions, i.e., $E(B - V) = 0$, $T_{\text{rel}} = 1$, and $X = 1$,

$$\frac{t_{\text{exp}}}{t_{\text{exp},0}} = \frac{N_{\text{eff}}}{N_{\text{eff},0}} \frac{1}{T_{\text{rel}}^2} \times 10^{0.8[K(X-1)+AE(B-V)]-0.4[m_{\text{sky}}-m_{\text{sky},0}]}, \quad (7)$$

where $N_{\text{eff},0}$ is obtained using Equation (6) with the nominal seeing $\sigma_{\text{see}} = 1.3''$. This estimate for the corrected exposure time (rounded up to the nearest integer) is used to set the duration of the upcoming exposure. Finally, *copilot* compares the depth, estimated from detected PS1 stars, attained by a given image to the desired depth, which is defined as

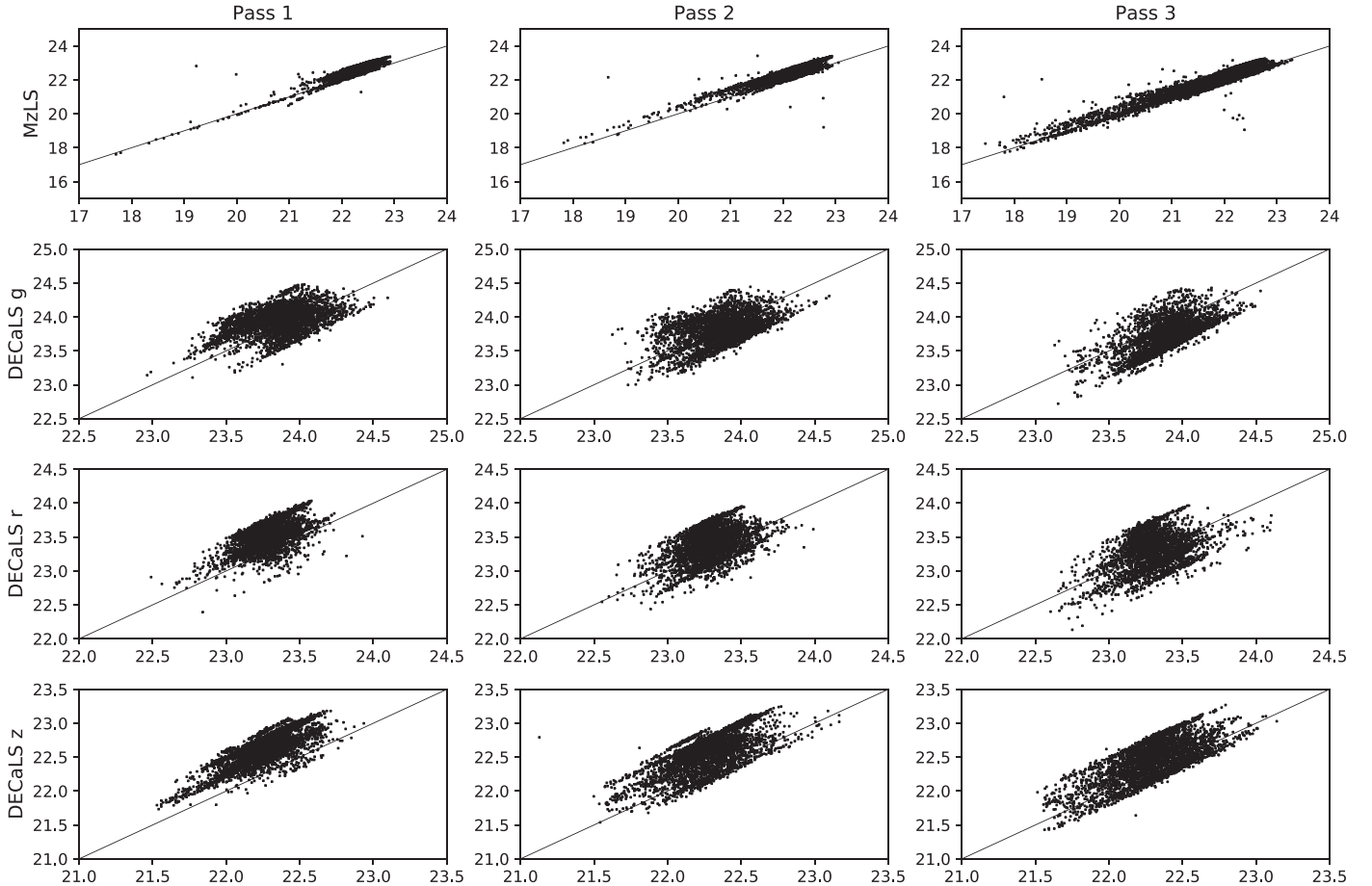


Figure 4. Depth (mag) comparison between the offline pipeline (x-axes) and obsbot estimate (y-axes).

detecting the canonical $0.45''$ exponential disk galaxy at $S/N = 5$, by computing the median m_{depth} of all detected sources. The success factor of the observation is presented as the exposure factor, $R_{\text{expfac}} \equiv t_{\text{observed}}/t_{\text{desired}}$, i.e., the ratio between the actual exposure time used for the image and the exposure time that would have been needed to reach depth. The exposure factor is reported on the graph that is visible to the observer.

Figure 4 shows the comparison between the obsbot depth estimate and the one determined by the offline pipeline. The two are well correlated but is tighter for Mosaic than DECam. obsbot tends to slightly overestimate the depth, especially for DECam, but this is a small effect and had no adverse effect for the overall depth of the surveys.

4.3. Implementation for MzLS

For each on-sky exposure that is written to disk, mosbot analyzes a single CCD amplifier to (a) determine the sky level, (b) detect sources and measure the FWHM, (c) match them to sources from the PanSTARRS1 catalog, (d) derive the zero-point of the image, (e) compare this zero-point to the fiducial zero-point to determine the transparency, and (f) derive the attained depth of the image. In addition, mosbot determines the airmass and Galactic extinction of the next pointing, predicts the band-dependent seeing based on an empirical relationship, and calculates the needed exposure time to reach depth using Equation (7).

mosbot only corrects the exposure time for upcoming observations; the pointing offset of the telescope (which is

computed and displayed by both mosbot and copilot) has to be corrected by the night-time observer, and is done while the exposure is reading out.

4.4. Implementation for DECaLS

At the start of the DECaLS survey, nightly observations began with nominal exposure times that the observers modified on hour timescales as conditions changed. On 2015 February 25, we started using copilot and decbot. Similarly to mosbot for MzLS, decbot uses the most recent raw image on the disk to predict the exposure time needed to reach the depth at the next pointing. Tiles with the earliest LMST are added to the queue while all tiles with LMST in the past are ignored.

While decbot and mosbot can also choose the pass number based on the derived conditions, the observers could force a pass in conditions that were at the limit between passes. This could be used to avoid large slews as the surveys progressed, which might have resulted in larger overheads and uneven completion rates in different passes.

With DECam, the slewing to the next pointing is simultaneous with reading out the CCD. On average, slewing is faster (about 30 s for less than 5°) than read out, so the next exposure usually begins before the image is built, compressed, and written to the disk. Only after the image is written can obsbot analyze the image and copilot provide an update to the exposure time. The observing software cannot change the

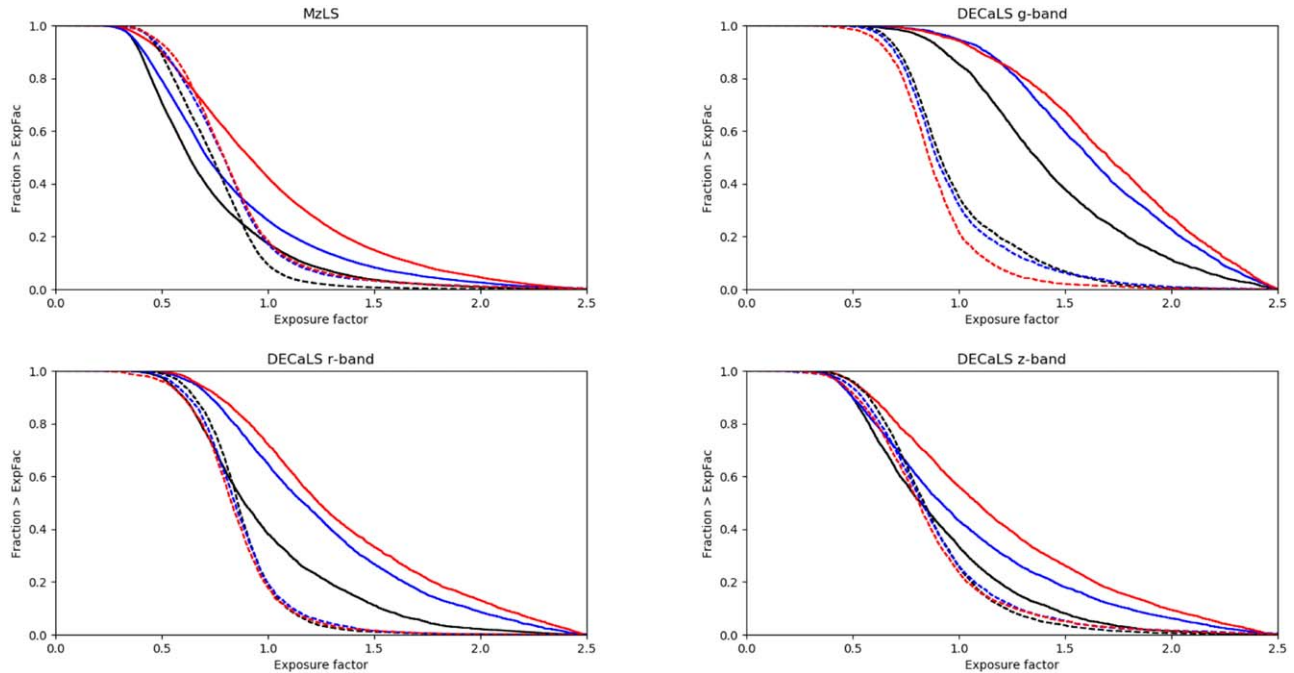


Figure 5. Reverse cumulative distribution of exposure factors for dynamically chosen exposure times (solid) and fixed fiducial exposure times under same observing conditions (dashed). Passes 1, 2, and 3 are in black, blue, and red, respectively.

exposure time once the exposure begins, so the exposure time would only be updated for the subsequent exposure.

As in the case of MzLS, *decbot* only corrects the exposure time for upcoming observations; the pointing offset of the telescope has to be corrected by the night-time observer by temporarily pausing the exposure queue.

4.5. Survey Efficiency Gains with Dynamic Observing

Dynamic exposure times allow the observations to compensate, ideally in real time, for the variable conditions to ensure that each image reaches depth. This is demonstrated in Figure 5, which shows the reverse cumulative distributions of the exposure factors for the Pass 1, 2, and 3 images in two cases: the actual MzLS and DECaLS images obtained under the dynamic exposure time operations, and what would have resulted if we had used our fiducial exposure time (see Table 3). In the case of the actual observations, we have restricted our selection to frames with exposure times between the minimum and maximum times allowed. In the case of the MzLS observations, the exposure time was corrected with a typical lag time corresponding to one frame; for DECaLS, this was two frames, due to the structure of the queuing software. Even so, the dynamic observation results in dramatic gains, especially in the cases of the Pass 2 and 3 observations which are obtained under nonphotometric and/or poor seeing conditions. In the case of the fixed exposure times, we would have had to reobserve a larger number of the shallow fields, resulting in extra on-sky observing time and extra overheads (primarily due to telescope slews, dome rotations, and CCD readouts). In addition to saving time by not underexposing, dynamic observing can save time by not exposing for longer than is necessary. This can be seen from Figure 6 which shows the relative depths of MzLS and DECaLS exposures using our dynamic exposure strategy versus what we would have achieved with fixed exposure times, either averaged over the whole survey or adjusted every night. The distributions for lags

of 1–2 exposures is much narrower around the prescribed depth than for the two fixed exposure time scenarios, especially in the case of the z band, for which there are long tails at high relative magnitudes.

5. Conclusions

We have presented the overall observing strategy used by the DECaLS and MzLS surveys, for which we implemented a novel approach of using a dynamic observing strategy, where the exposure times automatically varied in response to observing conditions in order to preserve uniformity of survey depth. We also implemented a strategy by which every position within the footprints of these surveys was targeted at least once under photometric conditions and at least once under conditions of good seeing. This method results in a demonstrably more uniform survey, which can be conducted optimally given a finite total amount of observing time and is better suited to cosmological studies near the depth limit of a survey. DECaLS and MzLS are the first surveys to use automated dynamic exposure times.

Dynamic exposure times may be crucial to future ground-based surveys, because they conserve telescope time and increase depth uniformity. The latter also improves searches for transients, such as moving objects, because non-varying transients should have a similar probability of detection in images taken at different epochs.

Our method currently necessitates lag times of 1–2 exposures, and removing this constraint would further improve uniformity of depth. Among surveys currently underway, the Hobby-Eberly Telescope Dark Energy Experiment (HETDEX) uses exposure times based on the conditions immediately before the start of the exposure (one of us (M.L.) developed an exposure time calculator and a next field selector for this survey and we confirmed, through private communication with an active member of the collaboration, that these were being used during operations). Based on the success described here, DESI

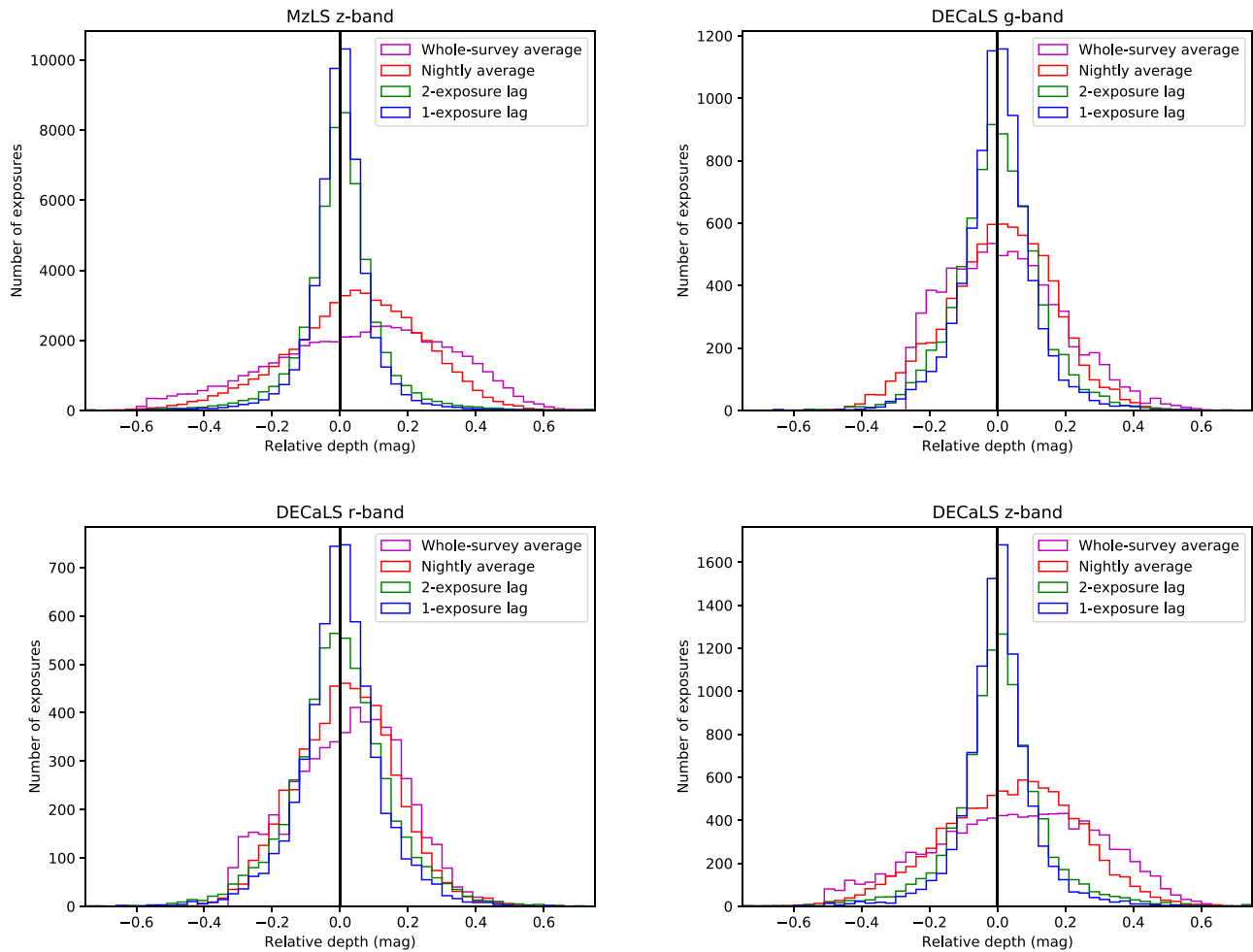


Figure 6. Histograms of relative depth for all dynamically observed MzLS and DECaLS images with exposure times within the allowed range. Both surveys had a 1–2 exposure lag, so blue and green lines show the relative depths we achieved with dynamic exposures. The purple and red lines show the relative depth distributions that would have resulted had we used a fixed exposure time equal to the average needed exposure time for the whole survey (purple) or that needed on a nightly basis (red). These latter distributions are significantly broader than the green histogram with many more outliers demonstrating that a fixed exposure approach would have resulted in a much less uniform survey.

is now planning to implement real-time dynamic exposures using contemporaneous measures of the seeing, transparency, and sky brightness.

The Legacy Surveys consist of three individual and complementary projects: the Dark Energy Camera Legacy Survey (DECaLS; NOAO Proposal ID no. 2014B-0404; PIs: D. Schlegel and A. Dey), the Beijing-Arizona Sky Survey (BASS; NOAO Proposal ID no. 2015A-0801; PIs: Z. Xu and X. Fan), and the Mayall z -band Legacy Survey (MzLS; NOAO Proposal ID no. 2016A-0453; PI: A.D.). DECaLS, BASS, and MzLS together include data obtained, respectively, at the Blanco telescope, Cerro Tololo Inter-American Observatory, NSF’s Optical-Infrared Astronomy Research Laboratory (NSF’s OIR Lab), the Bok telescope, Steward Observatory, University of Arizona, and the Mayall telescope, Kitt Peak National Observatory, NSF’s OIR Lab. The Legacy Surveys project is honored to be permitted to conduct astronomical research on Iolkam Du’ag (Kitt Peak), a mountain with particular significance to the Tohono O’odham Nation.

NSF’s OIR Lab is operated by the Association of Universities for Research in Astronomy (AURA) under a cooperative agreement with the National Science Foundation.

This project used data obtained with the Dark Energy Camera (DECam), which was constructed by the Dark Energy Survey (DES) collaboration. Funding for the DES Projects has been provided by the U.S. Department of Energy, the U.S. National Science Foundation, the Ministry of Science and Education of Spain, the Science and Technology Facilities Council of the United Kingdom, the Higher Education Funding Council for England, the National Center for Supercomputing Applications at the University of Illinois at Urbana-Champaign, the Kavli Institute of Cosmological Physics at the University of Chicago, Center for Cosmology and Astro-Particle Physics at the Ohio State University, the Mitchell Institute for Fundamental Physics and Astronomy at Texas A&M University, Financiadora de Estudos e Projetos, Fundacao Carlos Chagas Filho de Amparo, Financiadora de Estudos e Projetos, Fundacao Carlos Chagas Filho de Amparo a Pesquisa do Estado do Rio de Janeiro, Conselho Nacional de Desenvolvimento Científico e Tecnológico and the Ministerio da Ciencia, Tecnologia e Inovacao, the Deutsche Forschungsgemeinschaft and the Collaborating Institutions in the Dark Energy Survey. The Collaborating Institutions are Argonne National Laboratory, the University of California at Santa Cruz, the University of Cambridge, Centro de Investigaciones Energeticas,

Medioambientales y Tecnológicas-Madrid, the University of Chicago, University College London, the DES-Brazil Consortium, the University of Edinburgh, the Eidgenössische Technische Hochschule (ETH) Zurich, Fermi National Accelerator Laboratory, the University of Illinois at Urbana-Champaign, the Institut de Ciències de l’Espai (IEEC/CSIC), the Institut de Física d’Altes Energies, Lawrence Berkeley National Laboratory, the Ludwig-Maximilians Universität München and the associated Excellence Cluster Universe, the University of Michigan, the NSF’s Optical–Infrared Astronomy Research Laboratory, the University of Nottingham, the Ohio State University, the University of Pennsylvania, the University of Portsmouth, SLAC National Accelerator Laboratory, Stanford University, the University of Sussex, and Texas A&M University.

BASS is a key project of the Telescope Access Program (TAP), which has been funded by the National Astronomical Observatories of China, the Chinese Academy of Sciences (the Strategic Priority Research Program “The Emergence of Cosmological Structures” grant no. XDB09000000), and the Special Fund for Astronomy from the Ministry of Finance. The BASS is also supported by the External Cooperation Program of Chinese Academy of Sciences (grant no. 114A11KYSB20160057), and Chinese National Natural Science Foundation (grant no. 11433005).

The Legacy Survey team makes use of data products from the Near-Earth Object Wide-field Infrared Survey Explorer (NEOWISE), which is a project of the Jet Propulsion Laboratory/California Institute of Technology. NEOWISE is funded by the National Aeronautics and Space Administration.

The work of E.F.S. was performed under the auspices of the U.S. Department of Energy by Lawrence Livermore National Laboratory under Contract DE-AC52-07NA27344.

This research used resources of the National Energy Research Scientific Computing Center, a Department of Energy Office of Science User Facility supported by the Office of Science of the U.S. Department of Energy under Contract No. DE-AC02-05CH11231.

The Legacy Surveys imaging of the DESI footprint is supported by the Director, Office of Science, Office of High Energy Physics of the U.S. Department of Energy under Contract No. DE-AC02-05CH1123, by the National Energy Research Scientific Computing Center, a Department of Energy Office of Science User Facility under the same contract, and by the U.S. National Science Foundation, Division of Astronomical Sciences under Contract No. AST-0950945 to NSF’s OIR Lab.















A.D.M. was supported by the U.S. Department of Energy, Office of Science, Office of High Energy Physics, under Award Number DE-SC0019022.

J.M. gratefully acknowledges support from the U.S. Department of Energy, Office of Science, Office of High Energy Physics under Award Number DE-SC002008, and from the National Science Foundation under grant AST-1616414.

Finally, we would like to thank the anonymous referee, whose comments helped improve this paper.

Facilities: KPNO:Mayall (Mosaic3), Steward:Bok (90Prime), CTIO:Blanco (DECam), WISE, Gaia.

ORCID iDs

Martin Landriau  <https://orcid.org/0000-0003-1838-8528>
 Arjun Dey  <https://orcid.org/0000-0002-4928-4003>
 Dustin Lang  <https://orcid.org/0000-0002-1172-0754>
 David J. Schlegel  <https://orcid.org/0000-0002-5042-5088>
 Peter E. Nugent  <https://orcid.org/0000-0002-3389-0586>
 Robert Blum  <https://orcid.org/0000-0002-8622-4237>
 Douglas P. Finkbeiner  <https://orcid.org/0000-0003-2808-275X>
 David Herrera  <https://orcid.org/0000-0003-2092-6727>
 Stéphanie Juneau  <https://orcid.org/0000-0002-0000-2394>
 Ian McGreer  <https://orcid.org/0000-0002-3461-5228>
 Aaron M. Meisner  <https://orcid.org/0000-0002-1125-7384>
 John Moustakas  <https://orcid.org/0000-0002-2733-4559>
 Edward F. Schlafly  <https://orcid.org/0000-0002-3569-7421>
 Francisco Valdes  <https://orcid.org/0000-0001-5567-1301>
 Alistair R. Walker  <https://orcid.org/0000-0002-7123-8943>

References

- Abazajian, K. N., Adelman-McCarthy, J. K., Agüeros, M. A., et al. 2009, *ApJS*, **182**, 543
- Chambers, K. C., Magnier, E. A., Metcalfe, N., et al. 2016, arXiv:1612.05560
- DESI Collaboration, Aghamousa, A., Aguilar, J., et al. 2016a, arXiv:1611.00036
- DESI Collaboration, Aghamousa, A., Aguilar, J., et al. 2016b, arXiv:1611.00037
- Dey, A., Rabinowitz, D., Karcher, A., et al. 2016, *Proc. SPIE*, **9908**, 99082C
- Dey, A., Schlegel, D. J., Lang, D., et al. 2019, *AJ*, **157**, 168
- Flaugher, B., Diehl, H. T., Honscheid, K., et al. 2015, *AJ*, **150**, 150
- Gaia Collaboration, Brown, A. G. A., Vallenari, A., et al. 2016a, *A&A*, **595**, A2
- Gaia Collaboration, Prusti, T., de Bruijne, J. H. J., et al. 2016b, *A&A*, **595**, A1
- Hardin, R. H., Sloane, N. J. A., & Smith, W. D. 2012, Tables of Spherical Codes with Icosahedral Symmetry <http://neilsloane.com/icosahedral.codes/>
- The Dark Energy Survey Collaboration 2005, arXiv:astro-ph/0510346
- Williams, G. G., Olszewski, E., Lesser, M. P., & Burge, J. H. 2004, *Proc. SPIE*, **5492**, 787
- Wright, E. L., Eisenhardt, P. R. M., Mainzer, A. K., et al. 2010, *AJ*, **140**, 1868
- Zou, H., Zhou, X., Fan, X., et al. 2017, *PASP*, **129**, 064101